Properties of microscopic nucleus-nucleus interaction for molecular resonance formation in $^{12}C+^{12}C$ and $3\alpha+3\alpha$ systems

M. Ito,[1] Y. Sakuragi,[2] and Y. Hirabayashi[3]
[1]*Division of Physics, Graduate School of Science, Hokkaido University, Sapporo 060-0810, Japan*
[2]*Department of Physics, Osaka City University, Osaka 558-8585, Japan*
[3]*Center for Information and Multimedia Studies, Hokkaido University, Sapporo 060-0811, Japan*
(Received 11 December 2000; published 2 May 2001)

Properties of microscopic interaction potentials between two ^{12}C nuclei are discussed in connection with the formation of $^{12}C+^{12}C$ and $3\alpha+3\alpha$ molecular resonances. The nucleus-nucleus interactions are calculated by the double-folding procedure based on a realistic nucleon-nucleon interaction (DDM3Y) and microscopic ^{12}C transition densities calculated from 3α-RGM wave functions. The interaction potential can be written as the sum of the monopole part obtained from the monopole density and the multiple parts generated from the quadrupole component of the density. We discuss the role of the monopole and multipole parts of the potential separately. It is shown that the multipole part is very strong in the channels with $3\alpha+3\alpha$ structure and the energy positions of the $3\alpha+3\alpha$ molecular bands generated by the monopole potential are largely modified. The effect is moderate but non-negligible on the molecular bands with the $^{12}C+^{12}C$ dinuclearlike structure and largely modifies the band crossing diagram between the elastic and aligned-inelastic molecular bands. The channel coupling effect among the $^{12}C+^{12}C$ channels, namely, the elastic channel and the single- and mutual-2^+_1 excitation channels is also investigated. Due to the strong coupling between the ground and 2^+_1 states of ^{12}C, the resonance wave functions obtained by the coupled-channel calculation have an additional radial node compared with those of the single-channel resonances. All the results are discussed in connection with the band crossing model which was believed to be successful in describing the $^{12}C+^{12}C$ molecular resonances.

DOI: 10.1103/PhysRevC.63.064303 PACS number(s): 21.60.Gx, 24.10.Eq, 24.30.Gd, 25.70.Ef

I. INTRODUCTION

Since the first discovery of three sharp resonances in the $^{12}C+^{12}C$ collision near the Coulomb-barrier energies in the 1960s [1], a number of pronounced resonance phenomena have been observed in various reaction channels of many light heavy-ion systems, particularly of the $^{12}C+^{12}C$, $^{16}O+^{12}C$, and $^{16}O+^{16}O$ ones. Those resonances were observed not only around the Coulomb-barrier energies but also at energies well above the Coulomb barrier [2].

Among the heavy-ion systems, the $^{12}C+^{12}C$ system was the most extensively studied and many pronounced resonance structures were observed in the elastic and inelastic scattering leading to the 2^+_1 and 3^-_1-excited states of ^{12}C [3–6] and nucleon or alpha-particle transfer reactions well above the Coulomb barrier [7–12]. Various models are proposed in order to explain the resonance phenomena observed in the $^{12}C+^{12}C$ inelastic scattering well above the Coulomb barrier [13–22].

Many of the theoretical approaches were based on the coupled-channel approach or an approximate form of it such as distorted-wave theories and they looked successful to a certain level in reproducing the gross structure of the resonancelike behavior of excitation functions [13–22]. The so-called ''band crossing model'' (BCM) [13–15] is the simplest and superior to all other models in the sense that this model is able to predict the energy range and spins at which the resonances are to be observed. This model also explains the mechanism of the resonance formation in terms of the crossing between a dinuclear rotational (molecular) band of the elastic channel and those of inelastic channels. In BCM, the crossing between the elastic and inelastic molecular bands is realized by an effective increase of the moment of inertia of the inelastic ''aligned band'' due to the ''spin-alignment'' mechanism, namely, the lowering of the orbital angular momentum in the inelastic channel in which the intrinsic spins of the colliding nuclei has the stretched coupling with the orbital angular momentum. It also succeeded in reproducing and interpreting the experimental data of heavy-ion resonances not only in the $^{12}C+^{12}C$ system but also in the $^{16}O+^{12}C$ [16,17] and $^{16}O+^{16}O$ ones [18]. The resonance states observed in these heavy-ion systems are thus interpreted as the so-called ''molecular resonances'' in which two colliding nuclei keep touching their surfaces and rotate to each other by almost keeping their identities.

However, not only in BCM but also in other theoretical models, all the interactions between colliding nuclei were phenomenological ones such as the empirical optical potentials. As is well known, the empirical optical potentials for low-energy heavy-ion scattering have a substantial ambiguity in their depth and shape and, hence, it was inevitable that all these model calculations suffered from the ambiguity due to the use of the empirical interactions. Most of the empirical potentials used in the previous calculations are the so-called ''shallow potential,'' a typical value of the central depth being, say 20 MeV, which is supplemented by a repulsive core in the inner region for taking account of the Pauli exclusion Principle between the interacting nuclei. However, subsequent theoretical studies revealed that realistic heavy-ion potential was the so-called ''deep potential'' and had no repulsive core at short distance even when the Pauli principle was correctly taken into account [23,24]. The validity of the

''deep potential'' has now been established through the recent observation and analyzes of the nuclear-rainbow phenomena [25]. Thus, it is very important to reinvestigate the previous analyses of the heavy-ion resonance phenomena by using more realistic, ''deep'' interactions.

In addition to the above dinucleus resonances, another important discovery was reported on a new type of heavy-ion resonance which decays into multicluster exit channels. Namely, a broad resonancelike structure was observed in the $^{12}C+^{12}C$ inelastic scattering leading to the $^{12}C(0_2^+)+^{12}C(0_2^+)$ channel [26,27] at energies around $E_{c.m.}=32.5$ MeV. Since the 0_2^+ excited state at $E_x=7.65$ MeV in the ^{12}C nucleus is known to be a well-developed 3α cluster state [28–31], which itself is a sharp resonance state just above the $^{12}C \rightarrow 3\alpha$ breakup threshold at 7.27 MeV, the resonance observed in the $^{12}C(0_2^+)+^{12}C(0_2^+)$ channel should not be a simple dinucleus type molecular resonance state but it could be a state having a multicluster molecular configuration, such as the $3\alpha+3\alpha$ one. Moreover, in the recent experiment by Chappel *et al.* [32] and by Marechal *et al.* [33], resonance peaks have been observed also in other exit channels, such as $^{12}C(0_2^+)+^{12}C(3_1^-)$, $^{12}C(3_1^-)+^{12}C(3_1^-)$, and $^{8}Be_{g.s.}+^{16}O_{g.s.}$, around the same $E_{c.m.}=32.5$ MeV region with a good correlation to the above-mentioned resonance in the $^{12}C(0_2^+)+^{12}C(0_2^+)$ channel. On the other hand, it is well known that the pronounced resonance structure also exist in the $^{12}C_{g.s.}+^{12}C(0_2^+)$ channel around $E_{c.m.}=29.5$ MeV [34,35].

In order to understand the various resonance states with very different nuclear structure such as $^{12}C+^{12}C$, $^{12}C+3\alpha$, and $3\alpha+3\alpha$ one systematically, the coupled-channel calculation based on the realistic nucleus-nucleus interaction should be performed. Recently, a coupled-channel study called the microscopic coupled channel (MCC) has been made on the $^{12}C+^{12}C$ resonance reactions [36–38]. In the MCC calculation, the ^{12}C-^{12}C interactions are calculated in the double-folding (DF) model [39]. In this model, the real part of the interaction is calculated by folding the effective nucleon-nucleon (*NN*) interaction with the transition-density distributions of the two colliding ^{12}C nuclei, which leads to a typical ''deep potential'' interaction. The result of MCC calculation was quite successful in reproducing the resonance behavior of the cross sections not only in the channels with $^{12}C+^{12}C$ configuration but also in those with $^{12}C+3\alpha$ and $3\alpha+3\alpha$ one, of which magnitude is ranging from 100 mb to 10 μb [36–38]. This implies that the double-folding interactions used in the MCC calculation is reliable.

In the present paper, we discuss the properties of the microscopic nucleus-nucleus potentials same as those in the MCC calculation and investigate its effects on the resonance formation. These microscopic (DF model) interactions with the realistic *NN* interaction give reliable deep potentials and are free from any artificial parameters. The folded-diagonal density of excited states with a nonzero spin has the multipole parts which relate to the intrinsic deformation of a nucleus in addition to spherical (monopole) one. The microscopic DF potentials can be divided into two parts according to the classification of the folded densities. The first part is calculated by folding the monopole part of the diagonal densities, while the other one is done by folding the higher multipole part of the densities. Since the ^{12}C nucleus is strongly deformed [28–31], in the $^{12}C+^{12}C$ system, the molecular rotational bands generated by the former part are largely modified by the latter part. The molecular bands with the modification due to the multipole part are very different from those suggested in BCM [13–15], while those without the modification is similar to the bands in BCM. Furthermore, the channel coupling effect is strong due to the strong deformation of the ^{12}C nucleus and hence, the reaction dynamics is also different from that discussed in BCM based on the weak coupling picture.

In Secs. II and III, we describe the framework of MCC and show the properties of the nucleus-nucleus potentials in detail, respectively. The calculated molecular rotational bands having the $^{12}C+^{12}C$ and $3\alpha+3\alpha$ structure are shown in Sec. IV and V, respectively. In both sections, the effect of the potential originating from the deformation of ^{12}C is discussed in details. In Sec. VI, we discuss the roles of the channel coupling effect in the channels with the $^{12}C+^{12}C$ structure. The last section will be devoted to summary and discussion.

II. FRAMEWORK OF THE MICROSCOPIC COUPLED CHANNELS

A. Coupled-channel equations with microscopic interactions

In a practical calculation, the coupled-channels equations describing the collision of two nuclei for the total angular momentum of the system J

$$\left[-\frac{\hbar^2}{2\mu}\frac{d^2}{dR^2}+\frac{\hbar^2 L(L+1)}{2\mu R^2}+V^{(J)}_{\alpha L,\alpha L}(R)-E_\alpha\right]\chi^{(J)}_{\alpha L}(R) = -\sum_{(\beta,L')\neq(\alpha,L)} V^{(J)}_{\alpha L,\beta L'}(R)\chi^{(J)}_{\beta L'}(R), \quad (1)$$

are solved numerically. Here, α denotes a ''channel'' designated by the intrinsic spins of two nuclei I_1 and I_2, the channel spin $I(\mathbf{I}_1+\mathbf{I}_2=\mathbf{I})$ and the sum of the excitation energies of two nuclei ϵ_α. Thus, $E_\alpha \equiv E-\epsilon_\alpha$ is the center-of-mass (c.m.) energy of the nucleus-nucleus relative motion in the channel α. For a given J, a channel specified by α contains several ''subchannels'' specified by α and L satisfying $|J-I|\leq L\leq J+I$, where L is the orbital angular momentum associated to the relative coordinate $\mathbf{R}$. In this paper, we call a state specified by α and L a ''subchannel'' and one specified by α (or a combination of I_1 and I_2) a ''channel.'' The distinction between channel and subchannel is very important in this paper. In Eq. (1), $\chi^{(J)}_{\alpha L}(R)$ represents the radial wave function of the relative motion in the subchannel αL.

All the diagonal $[(\alpha L)=(\beta L')]$ and coupling $[(\alpha L)\neq(\beta L')]$ potentials $V^{(J)}_{\alpha L,\beta L'}(R)$ are calculated by the double-folding (DF) model [39] and defined as

$$V^{(J)}_{\alpha L,\beta L'}(R)=V^{(J)}_{I_1I_2IL,I_1'I_2'I'L'}(R)$$
$$=\langle\Phi^{(JM)}_{I_1I_2IL}(\xi_1,\xi_2,\hat{\mathbf{R}})|\times\sum_{\substack{i\in C_1\\ j\in C_2}}v_{NN}(\mathbf{x}_{ij})|\Phi^{(JM)}_{I_1'I_2'I'L'}(\xi_1,\xi_2\hat{\mathbf{R}})\rangle_{\xi_1,\xi_2,\hat{\mathbf{R}}}. \tag{2}$$

Here $\Phi^{(JM)}_{\alpha L}(\xi_1,\xi_2,\hat{\mathbf{R}})$ is the channel wave function. In an identical boson system, the explicit form of the channel wave function $\Phi^{(JM)}_{\alpha L}(\xi_1,\xi_2,\hat{\mathbf{R}})$ is written as

$$\Phi^{(JM)}_{I_1I_2IL}(\xi_1,\xi_2,\hat{\mathbf{R}})$$
$$=\sqrt{\frac{1}{2(1+\delta_{I_1I_2}\delta_{i_1i_2})}}\mathcal{S}_{12}[[\psi^{(i_1)}_{I_1}\times(\xi_1)\otimes\psi^{(i_2)}_{I_2}(\xi_2)]_I\otimes i^LY_L(\hat{\mathbf{R}})]_{JM}$$
$$=\sqrt{\frac{1}{2(1+\delta_{I_1I_2}\delta_{i_1i_2})}}\times\{[[\psi^{(i_1)}_{I_1}(\xi_1)\otimes\psi^{(i_2)}_{I_2}(\xi_2)]_I\otimes i^LY_L(\hat{\mathbf{R}})]_{JM}$$
$$+[[\psi^{(i_1)}_{I_1}(\xi_2)\otimes\psi^{(i_2)}_{I_2}(\xi_1)]_I\otimes(-1)^Li^LY_L(\hat{\mathbf{R}})]_{JM}\} \tag{3}$$

which is symmetrized with respect to the exchange of the identical nuclei. Here ξ_1 and ξ_2 represent the internal coordinates of the individual nuclei, while R and $\hat{\mathbf{R}}$ denote the radial and angular parts of the relative coordinate between the center of mass (c.m.) of the colliding nuclei. $\mathcal{S}_{12}$ denotes the symmetrization operator which exchange the two identical nuclei, namely, the exchange of whole nucleons between two nuclei. This kind of exchange term only appears in a system composed of two identical nuclei. This corresponds to one of the various nucleon-exchange terms appearing in a fully antisymmetrized resonating-group-method (RGM) wave function describing the identical boson system. In Eq. (3), $\psi^{(i_1)}_{I_1}(\xi_1)$ denotes the internal wave function of a nucleus in the i_1th state with an intrinsic spin I_1: e.g., a state with $i_1=2$ and $I_1=0^+$ implies the 0^+_2 state.

In Eq. (2), $v_{NN}(\mathbf{x}_{ij})$ represents an effective nucleon-nucleon interaction which acts between the ith nucleon in a nucleus C_1 and the jth one in the other nucleus C_2. A more explicit expressions of Eq. (2) will be given in the next subsection. We use the DDM3Y (density-dependent Michigan three-range Yukawa interaction) [40,41] as the nucleon-nucleon (NN) interaction. The interaction has the following factorized form:

$$v_{NN}(E,\rho;\mathbf{s})=g(E,\mathbf{s})f(E,\rho). \tag{4}$$

Here, $f(E,\rho)$ is a density dependent factor with a form of

$$f(E,\rho)=C(E)[1+\alpha(E)e^{-\beta(E)\rho}], \tag{5}$$

while $g(E,s)$ is the spin- and isospin-scalar ($S=T=0$) component of the original M3Y interaction [42]. Here E denotes an incident energy per nucleon in a laboratory system. The coefficients $C(E)$, $\alpha(E)$, and $\beta(E)$ in the density-dependent factor $f(E,\rho)$ were determined at each energy by fitting a volume integral of the $v_{NN}(E,\rho{:}s)$ to the real part of the optical potential felt by a nucleon in the nuclear matter [43]. The inclusion of the density dependence is very important, especially for describing a large difference of interactions between two nuclei in various states having different nuclear structure. For example, the interaction between the two nuclei both in the spatially compact ground state and that between nuclei both in the spatially extended excited state is very different and the use of the density-dependent effective NN interaction is essential in order to correctly take account of such differences due to the structure change.

The coupling potential for the Coulomb excitation is also given by the folding model by just replacing the NN nuclear interaction v_{NN} with the NN Coulomb one in Eq. (2). However, the inclusion of the Coulomb coupling is not essential in the lighter heavy-ion systems.

B. Microscopic nucleus-nucleus interaction

By substituting Eq. (3) into Eq. (2), the expression for the coupling potential in Eq. (2) reduces to the following form:

$$V^{(J)}_{I_1I_2IL,I_1'I_2'I'L'}(R)$$
$$=\sqrt{\frac{1}{(1+\delta_{I_1,I_2})(1+\delta_{I_1',I_2'})}}\times\sum_{\lambda}\hat{I}\hat{L}\hat{L}'(-1)^{1/2(L-L'+\lambda)}W(ILI'L';J\lambda)$$
$$\times\langle L0L'0|\lambda0\rangle\{\tilde{V}^{(\lambda)}_{I_1I_2I,I_1'I_2'I'}(R)+(-1)^{I'}\tilde{V}^{(\lambda)}_{I_1I_2I,I_2'I_1'I'}(R)\}. \tag{6}$$

Here, $W(ILI'L';J\lambda)$ represents the ordinary Racah coefficient and $\hat{I},\hat{L},\ldots$, are abbreviations of $\sqrt{2I+1},\sqrt{2L+1},\ldots$. [We have dropped the superscripts i_1 and i_2 appearing in Eq. (3) for simplicity. Hereafter, we do the same for simplicity of notations.] In Eq. (6), $\tilde{V}^{(\lambda)}_{I_1I_2I,I_1'I_2'I'}(R)$ denotes the form factor having the following form:

$$\tilde{V}^{(\lambda)}_{I_1I_2I,I_1'I_2'I'}(R)$$
$$=\hat{I}_1\hat{I}_2\sum_{\lambda_1\lambda_2}\hat{I}\hat{I}'\hat{\lambda}_1\hat{\lambda}_2\begin{pmatrix}I_1 & I_2 & I\\ I_1' & I_2' & I'\\ \lambda_1 & \lambda_2 & \lambda\end{pmatrix}(-1)^{\lambda_1}(2\pi)^{3/2}$$
$$\times\langle\lambda_10\lambda_20|\lambda0\rangle C(E)\int_0^\infty dkk^2\overline{v(k)}j_\lambda(kR)$$
$$\times\{\overline{\rho}^{(\lambda_1)}_{I_1,I_1'}(k)\overline{\rho}^{(\lambda_2)}_{I_2,I_2'}(k)+\alpha(E)\tilde{\rho}^{(\lambda_1)}_{I_1I_1'}(k)\tilde{\rho}^{(\lambda_2)}_{I_2,I_2'}(k)\}. \tag{7}$$

Here $\alpha(E)$ and $C(E)$ are the same as those in Eq. (5). In the case of the Coulomb interaction, one should replace v_{NN} by the *NN* Coulomb potential and let $C(E)=1$ and $\alpha(E)=0$ in Eq. (7). On the right-hand side of Eq. (7), $j_\lambda(kR)$ represents a spherical Bessel function of the rank λ. The $\overline{v(k)}$ and $\overline{\rho}^{(\lambda)}_{I,I'}(k)[\tilde{\rho}^{(\lambda)}_{I,I'}(k)]$ represent a Fourier transform of the v_{NN} and the transition density (modified transition density) which are defined below.

The diagonal or transition density of colliding nucleus at a position $\mathbf{r}$ with respect to the c.m. of the nucleus are expanded into multipole components as follows:

$$\rho_{IK,I'K'}(\mathbf{r})=\langle\psi_{IK}(\xi)|\sum_{k=1}^{A}\delta(\mathbf{r}-\mathbf{r_k})|\psi_{I'K'}(\xi)\rangle$$

$$=\sum_{\lambda,\mu}\langle I'K'\lambda\mu|IK\rangle\rho^{(\lambda)}_{I,I'}(r)[iY_{\lambda,\mu}(\hat{\mathbf{r}})]^*. \quad (8)$$

Here, $\psi_{IK}(\xi)$ represents the internal wave function of colliding nucleus obtained by the microscopic calculation such as resonating group method (RGM). Therefore, the nucleus-nucleus interactions expressed by Eqs. (6) and (7) are determined in a parameter free way, provided that the microscopic internal wave functions of colliding nuclei are given.

The Fourier transforms of the nucleon-nucleon interaction and the radial part of the transition densities, $\overline{v(k)}$, $\rho^{(\lambda)}_{I,I'}(k)$, and $\tilde{\rho}^{(\lambda)}_{I,I'}(k)$, are defined as

$$\overline{v(k)}=\sqrt{\frac{2}{\pi}}\int_0^\infty drr^2 j_0(kr)v_{NN}(r), \quad (9)$$

$$\overline{\rho}^{(\lambda)}_{I,I'}(k)=\sqrt{\frac{2}{\pi}}\int_0^\infty drr^2 j_\lambda(kr)\rho^{(\lambda)}_{I,I'}(r), \quad (10)$$

$$\tilde{\rho}^{(\lambda)}_{I,I'}(k)=\sqrt{\frac{2}{\pi}}\int_0^\infty drr^2 j_\lambda(kr)\hat{\rho}^{(\lambda)}_{I,I'}(r). \quad (11)$$

Here, $\hat{\rho}^{(\lambda_1)}_{I,I'}(r)$ represents a ''modified'' density associated to the density-dependent term of the DDM3Y interaction and defined by

$$\hat{\rho}^{(\lambda)}_{I,I'}(r)=\rho^{(\lambda)}_{I,I'}(r)e^{-\beta(E)\rho(r)}. \quad (12)$$

Here, $\rho(r)$ in the exponent is taken to be $\rho(r)=\rho^{(0)}_{I,I}(r)$ when $I'=I$ and $\rho(r)=\frac{1}{2}\{\rho^{(0)}_{I,I}(r)+\rho^{(0)}_{I',I'}(r)\}$ when $I'\neq I$. The v_{NN} in Eq. (9) is equal to either the M3Y interaction $g(E,\mathbf{s})$ when we calculate the nuclear interactions or to the Coulomb potential when we calculate the Coulomb interactions.

III. PROPERTIES OF MICROSCOPIC NUCLEUS-NUCLEUS POTENTIALS

In this section, we show the properties of the nucleon densities of ^{12}C calculated microscopically and discuss the features of the double-folding potentials calculated from the densities. The potential for the inelastic channel with a nonzero intrinsic spin has a slightly complicated structure.

The nuclear states of ^{12}C up to about 15 MeV excitation energy can be divided into two group of states according to their nuclear structure [28–31]. The first group of states are the so-called ''shell-model-like states'' having a spatially compact structure and the second ones are the ''3α-cluster states'' having a well-developed 3α structure. The 0^+_1 ground state, the 2^+_1(4.44 MeV) first excited state, and the 3^-_1(9.64 MeV) state belong to the first group, while the 0^+_2(7.65 MeV), 2^+_2(10.3 MeV), and 0^+_3(14.04 MeV) states belong to the second group [28,29]. The 2^+_2 and 0^+_3 states have not been identified experimentally due to the large widths. However, most cluster-model theories predict the existence of these states in this energy region above the 0^+_2 state.

A. Microscopic transition densities of ^{12}C

According to Eq. (8), the multipole expansion for the diagonal density ($I=I'$) can be divided into the monopole ($\lambda=0$) part and the $\lambda\neq0$ multipole one as follows:

$$\rho_{IK,IK'}(\mathbf{r})=\langle\Psi_{IK}(\xi)|\sum_{k=1}^{12}\delta(\mathbf{r}-\mathbf{r_k})|\psi_{IK'}(\xi)\rangle$$

$$=\sum_{\lambda,\mu}\langle IK'\lambda\mu|IK\rangle\rho^{(\lambda)}_{I,I}(r)[(iY_{\lambda,\mu}(\hat{\mathbf{r}})]^*$$

$$=\frac{1}{\sqrt{4\pi}}\rho^{(0)}_{I,I}(r)\delta_{K,K'}+\sum_{\lambda,\mu\neq0}\langle IK'\lambda\mu|IK\rangle\rho^{(\lambda)}_{I,I}(r)$$

$$\times[iY^*_{\lambda,\mu}(\hat{\mathbf{r}})]^*. \quad (13)$$

Here, the first term in the RHS of Eq. (13) is the spherical (monopole) part of the density distribution, while the rest terms are the nonspherical (multipole) parts, which exist in the state with a nonzero intrinsic spin.

As for the internal wave function of ^{12}C, $\psi_{IK}(\xi)$, we adopt the internal wave function calculated by Kamimura by the 3α-RGM method [31]. Transition densities obtained from the 3α-RGM wave functions were shown to well reproduce the observed level structure, the electric transition probabilities $[B(E\lambda)]$, and the charge form factors of the electron scattering [31].

Figures 1(a) and 1(b) show the density profiles of the shell-model-like states (0^+_1 and 2^+_1) and the 3α-cluster ones (0^+_2 and 2^+_2), respectively. Since a spinless state has only a $\lambda=0$ spherical density, there exists only a $\lambda=0$ density in the ground 0^+_1 and 0^+_2 states, which are shown by the solid curves in the upper panel of each figure. The density of the state having a nonzero intrinsic spin such as the 2^+_1 and 2^+_2 states has the nonspherical ($\lambda\neq0$) component of the density in addition to the spherical one. In the lower pannel of each figure, the $\lambda=0$ and $\lambda=2$ components of the density are shown by the solid and dashed curves, respectively.

As can be understood from Eq. (13), there should also exist the $\lambda=4$ component in the density of the 2^+ states. However, we neglect this component in the present paper, because the magnitude of the higher-multipolarity compo-

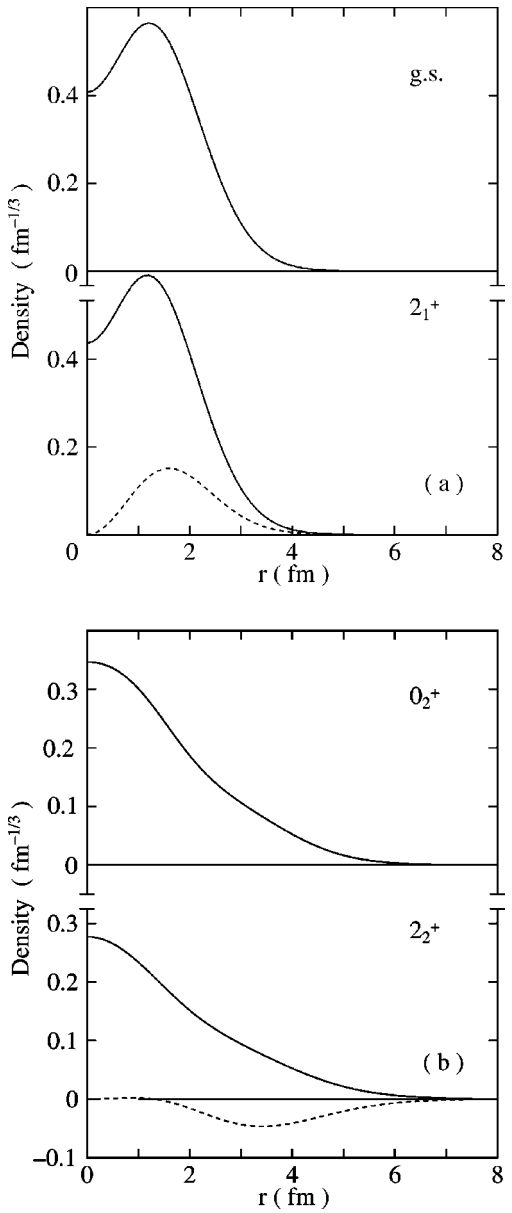

FIG. 1. (a) The diagonal density of the ground and 2_1^+ state in the ^{12}C nucleus. The ordinate denotes the modulus of the density. In the upper and lower panels of the figure, the density distribution of the ground and 2_1^+ states are shown, respectively. For the 2_1^+ state, the solid and dotted curves represent the monopole ($\lambda=0$) and quadrupole ($\lambda=2$) components, respectively. (b) The same as (a) but for the 0_2^+ and 2_2^+ states in the ^{12}C nucleus.

nents is found to be negligibly small. It is clearly seen in the figure that the radial shape of the densities of the 3α states (0_2^+ and 2_2^+) is more spatially extended than that of the shell-model-like states. The long-range nature of the latter has important effects on the calculated potentials.

B. Properties of microscopic potentials

The potentials calculated by the double-folding procedure can be divided into two parts according to the existence of the nonspherical density components in Eq. (13). We have given the expression for the double-folding potential in Eqs. (6) and (7) by the Fourier-transformation form. In the expression, one takes the summation over the three kinds of multipole variables λ_1, λ_2, and λ. λ_1 and λ_2 represent the multipole valuables for the density of individual nuclei 1 and 2, each of which corresponds to the multipolarity λ appearing in Eq. (13), while the λ in Eqs. (6) and (7) represents the total multipolarity satisfying a vector-coupling condition $|\lambda_1-\lambda_2|\leqslant\lambda\leqslant\lambda_1+\lambda_2$. The expression for the potential can be divided into two parts as follows:

$$V^{(J)}_{I_1I_2IL,I_1I_2I,L}(R)=\mathcal{V}^{(0)}_{I_1I_2,I_1I_2}(R)+\mathcal{N}_{12}{\sum_{\lambda}}' K(IL,IL;J\lambda)\times\{\hat{V}^{(\lambda)}_{I_1I_2I,I_1'I_2'I'}(R)+(-1)^{I'}\tilde{V}^{(\lambda)}_{I_1I_2I,I_2'I_1'I'}(R)\}. \quad (14)$$

Here, $\mathcal{N}_{12}$ represents the normalization constant in Eq. (6) with respect to the symmetrization between identical nuclei and the $K(IL,IL;J\lambda)$ does the factor including the Racah and Clebsh-Gordan coefficients and so on appearing in the summation of Eq. (6). The prime appearing in the summation implies that the $\lambda_1=\lambda_2=\lambda=0$ term are excluded from the summation. The first term $\mathcal{V}^{(0)}_{I_1I_2,I_1I_2}(R)$ corresponds to the $\lambda_1=\lambda_2=\lambda=0$ term in Eqs. (6) and (7) and its explicit expression reads

$$\mathcal{V}^{(0)}_{I_1I_2,I_1I_2}(R)=C(E)(2\pi)^{3/2}\int_0^\infty dk k^2\overline{v}(k)j_0(kR)\times\{\overline{\rho}^{(0)}_{I_1,I_1}(k)\overline{\rho}^{(0)}_{I_2,I_2}(k)+\alpha(E)\tilde{\rho}^{(0)}_{I_1,I_1}(k)\tilde{\rho}^{(0)}_{I_2,I_2}(k)\}, \quad (15)$$

where $\overline{\rho}^{(0)}_{I,I}(k)$ and $\tilde{\rho}^{(0)}_{I,I}(k)$ represent the Fourier-transform of the monopole densities defined in Eqs. (10) and in (11), respectively. This term is calculated only from the $\lambda_i=0$ ($i=1$ and 2) part of the density and nothing but the usual double-folding potential between spinless particles [44].

Since only the monopole part ($\lambda_i=0$) exists in the nucleon density of the spinless state, such as the ground state of even-even nuclei, only the first term in Eq. (14) contributes to the potential for the $0^+ + 0^+$ channels. For the inelastic channels containing the nonzero spin states, such as the $0^+ + 2^+$ and $2^+ + 2^+$ ones, the second term in Eq. (14) also contributes to the potentials, because of the $\lambda_i=2$ part of the density in the 2^+ state.

Moreover, there is a distinctly different feature between the first and the second term in Eq. (14). The first term depends only on the combination of intrinsic states of interacting nuclei, (I_1I_2) and independent of either the channel spin I, the orbital angular momentum L or the total angular momentum J. However, the second term depends also on I, L, and J. This implies that the nucleus-nucleus interactions of different subchannels are different from each other even though they consist of a common intrinsic-state channel α for a given J.

The above properties of the potentials are quite general and do not depend on the system. In the present paper, we take the $^{12}C+^{12}C$ system as an example and discuss the effect of the nonspherical-density part in Eq. (14) and the properties of the molecular bands generated by the potentials. Since the intrinsic deformation of the ^{12}C nucleus is very strong [28–31], this system is a typical example in which the effect of the nonspherical-density part is prominent.

In this paper, we consider two kinds of channel groups: The first group is the elastic channel $(0_1^+ + 0_1^+)$ and the inelastic $0_1^+ + 2_1^+$ and $2_1^+ + 2_1^+$ channels. The second group is the $0_2^+ + 0_2^+$, $0_2^+ + 2_2^+$, and $2_2^+ + 2_2^+$ channels. The former three channels have $^{12}C+^{12}C$ structure, while the latter three channels have a well-developed $3\alpha + 3\alpha$ structure. These channels are known to play important roles in the $^{12}C+^{12}C$ inelastic scattering leading to the mutual-0_2^+ excitation channel [45]. We refer to the first three channels and the second three ones as the ''shell group'' (SG) and the ''cluster group'' (CG), respectively.

There exists only the first term of Eq. (14) in the spinless channels such as the $0_1^+ + 0_1^+$ and $0_2^+ + 0_2^+$ ones, while both terms of Eq. (14) exist in the channels with nonzero intrinsic spins such as $0_1^+ + 2_1^+$, $2_2^+ + 2_2^+$. Figures 2(a) and 2(b) show the potentials for the $[2_1^+ \otimes 2_1^+]_{I=4,L=J-4}$ and $[2_2^+ \otimes 2_2^+]_{I=4,L=J-4}$ subchannels, respectively. The solid curve represents the potential calculated from Eq. (14), while the dotted and dashed ones-represent the individual contribution from Eq. (14). The former and latter curves represent the first and second terms of Eq. (14), respectively. All the curves include the Coulomb potentials calculated by the double-folding procedure. The sign of the second term of Eq. (14) shown by the dashed curves in Figs. 2(a) and 2(b) are opposite to each other. This originates from the difference of sign in the quadrupole $(\lambda = 2)$ density between the 2_1^+ and 2_2^+ states. The quadrupole density for the 2_1^+ state [Fig. 1(a)] is positive, while that for the 2_2^+ [Fig. 1(b)] is negative.

As can be seen from both figures, the contribution from the second term in Eq. (14) has a surface-peaked shape. The second term for the $[2_1^+ \otimes 2_1^+]_{I=4}$ channel is repulsive at the surface region which amounts to about 8 MeV around $R = 3.8$ fm, while that for the $[2_2^+ \otimes 2_2^+]_{I=4}$ channel is strongly attractive which reaches its maximum value of about 13 MeV around $R = 4$ fm. Since the centrifugal potential is strongly damped at the outer-side region, the contribution from the second term gives rise to a considerable change in the barrier-top resonance energy generated by the potential calculated with Eq. (15).

In both subchannels, the contribution of the second term of Eq. (14) gives rise to a visible change in the potential. In particular, the second term of Eq. (14) in the $[2_2^+ \otimes 2_2^+]_{I=4,L=J-4}$ subchannel is much stronger than that in the $[2_1^+ \otimes 2_1^+]_{I=4,L=J-4}$ one. This is due to the strong deformation of the 2_2^+ state with a well-developed 3α structure as shown in Fig. 1(b). Therefore, the change of the resonance energy due to the inclusion of the second term becomes more important in the $2_2^+ + 2_2^+$ channel having $3\alpha + 3\alpha$ structure.

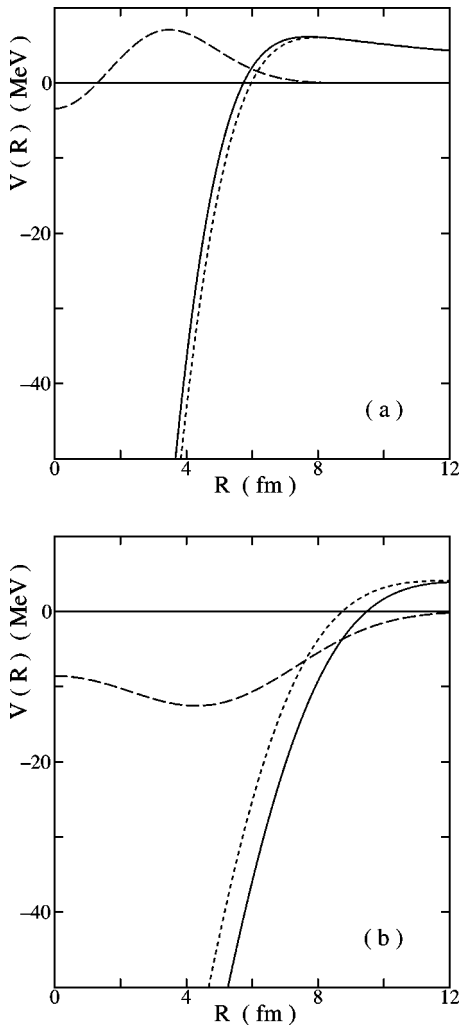

FIG. 2. (a) The potentials of the $[2_1^+ \otimes 2_1^+]_{I=4,L=J-4}$ subchannel for $J = 18$. The solid curve represents the full potentials calculated from Eq. (14), while the dashed and dotted ones represent the individual contributions of Eq. (14). All the curves include the Coulomb potentials calculated by the double-folding procedure. See text for details. (b) The same as (a) but for the $[2_2^+ \otimes 2_2^+]_{I=4,L=J-4}$ subchannel.

For later convention, let us call the sum of the nuclear and Coulomb potentials consisting of the first term in Eq. (14) alone the ''monopole potential,'' while we call the potential defined by the second term in Eq. (14) the ''higher-multipole potential.'' In the following sections, we discuss the nature of the molecular bands composed of the barrier-top resonances generated by the monopole potentials and the effects of the second term in Eq. (14) on the molecular bands.

IV. $^{12}C+^{12}C$ MOLECULAR BANDS

In this section, we show the potentials in the shell group (SG) and discuss the behavior of the molecular bands generated by the potentials. In Fig. 3, we show the monopole potentials (nuclear+Coulomb) in the $0_1^+ + 0_1^+$, $0_1^+ + 2_1^+$, and $2_1^+ + 2_1^+$ channels. These potentials are very closed to each other. This is because of the similarity of the monopole

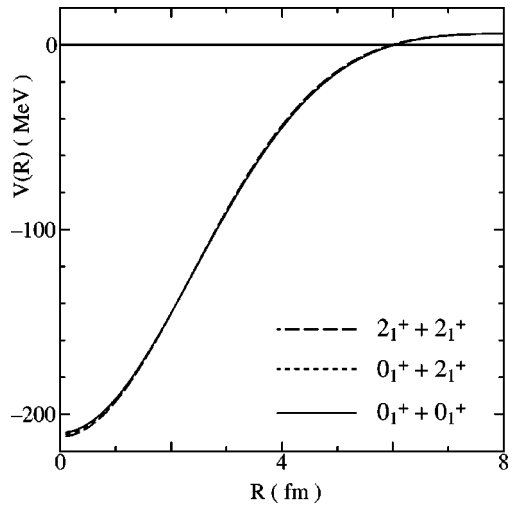

FIG. 3. The monopole part of the potentials for the elastic, $0_1^+ + 2_1^+$, and $2_1^+ + 2_1^+$ channels, which are shown by the solid, short-dashed, and long-dashed curves, respectively. In all the curves, the Coulomb part of the potential is included.

density distribution of the ground state and that of the 2_1^+ one as shown in Fig. 1. The effective potential which is the sum of the monopole potential and the centrifugal potential generates the molecular bands, i.e., the sequence of the potential resonances around the barrier top in each partial wave.

In the $[2_1^+ \otimes 2_1^+]_{I=4}$ channel, there are five subchannels, orbital angular momenta of which equal to $L=J\pm4$, $L=J\pm2$, and $L=J$ according to the angular-momentum coupling between the channel spin ($I=4$) and L. The $L=J\pm3$ and $L=J\pm1$ subchannels are forbidden by the parity-conservation law.

The molecular bands in the elastic $(0_1^+ + 0_1^+)$ and $[2_1^+ \otimes 2_1^+]_{I=4}$ channels are shown in Fig. 4(a). All the bands are calculated from the monopole potential. The abscissa and ordinate in the figure denote the $J(J+1)$ value and the total energy of the $^{12}C+^{12}C$ system with respect to the $^{24}Mg \rightarrow ^{12}C+^{12}C$ threshold energy, respectively. The band with double circles and solid circles corresponds to the molecular bands in the $L=J-4$ and $L=J-2$ subchannels, respectively, while the solid triangles and solid diamonds correspond to the bands in the $L=J+4$ and $L=J+2$ subchannels, respectively. The former two subchannels are called the ''aligned subchannel,'' while the latter two are called the ''antialigned subchannel.'' All the molecular bands shown here are members of $N=18$ rotational band, where N is the total oscillator-quantum number of the harmonic oscillator defined by $N=2n+L$. Here, n represents the number of nodes of the radial wave function.

The energy position of the molecular band in the $[2_1^+ \otimes +2_1^+]_{I=4,L=J}$ channels, shown by the open squares, is higher than that of the elastic-channel band by the intrinsic excitation energy 8.88 MeV and both bands are almost parallel to each other. This is because the monopole potentials of these channels are very closed to each other, which is due to the similarity of the monopole density distribution of the ground state and that of the 2_1^+ one (Figs. 1 and 3). The only difference of the effective potential among the five subchannels belonging to the $[2_1^+ \otimes 2_1^+]_{I=4}$ channel is the difference of the centrifugal potential, because the monopole part of the potentials is common to all the subchannels. Therefore, the resonance energies of the aligned band are the same as those of the $L=J$ band shifted to the higher-J side by four units of $\hbar$ for the $L=J-4$ band and by two units of $\hbar$ for the $L=J-2$ band. The antialigned band is obtained by the $L=J$ bandshifted to the lower-J side by four units of $\hbar$ for the $L=J+4$ band and by two units of $\hbar$ for the $L=J+2$ one.

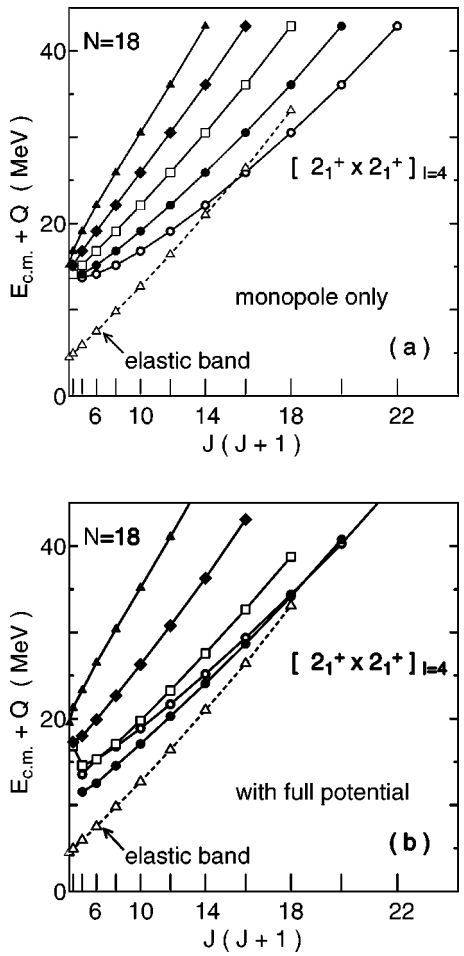

FIG. 4. (a) The molecular bands in the $[2_1^+ \otimes 2_1^+]_{I=4,L}$ subchannel. The double circles, solid circles, open squares, solid diamonds, and solid triangles represent the band in the $L=J-4$, $L=J-2$, $L=J$, and $L=J+2$, $L=J+4$ subchannels, respectively. (b) The same as (a) but for the molecular bands calculated from the full potentials. In both figures, the elastic molecular band is also shown by the short-dashed line with open triangles.

The molecular bands with $L \leqslant J$ in the $0_1^+ + 2_1^+$ and $2_1^+ + 2_1^+$ channels are shown in Fig. 5(a). The molecular band in the $[0_1^+ \otimes 2_1^+]_{I=2,L=J}$ subchannel is also parallel to the $0_1^+ + 0_1^+$ molecular band, the energy position of which is higher than that of the elastic band by the intrinsic excitation energies 4.44 MeV. As can be seen in Fig. 5(a), the ''band crossing'' between the aligned-inelastic molecular band and the elastic one occurs around $J=14$ and 16.

The band crossing between the elastic band and the

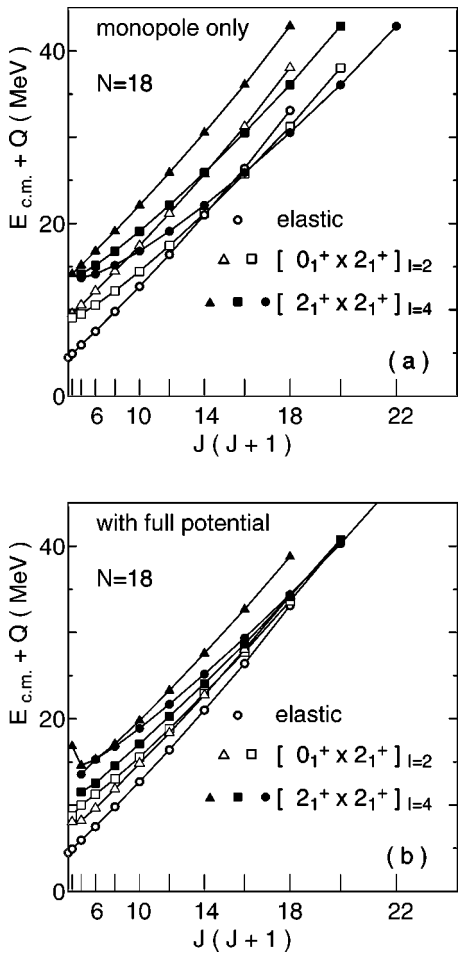

FIG. 5. (a) The molecular bands in the elastic ($[0_1^+\otimes 0_1^+]$), $[0_1^+\otimes 2_1^+]_{I=2,L}$ (with $L=J-2$, J) and $[2_1^+\otimes 2_1^+]_{I=4,L}$ (with $L=J-4$, $J-2$, J) subchannels, which are shown by the double circles, open squares, open triangles, solid circles, solid squares, and solid triangles, respectively. All the molecular bands are calculated from the monopole potentials. (b) The same as (a) but for the molecular bands calculated from the full potentials.

aligned-inelastic band in the present double folding potential is similar to the result of the band-crossing-model (BCM) calculation [13,14]. In the previous work based on BCM, however, ''shallow potentials,'' the central depth of which is about 20 MeV, were used as the nucleus-nucleus real potential which is very different from the double-folding-model potential used in the present work, the central depth of which is about 200 MeV. In the former case, the number of radial nodes in a molecular band is common to all J, which is zero. In the latter case, however, each of the molecular bands has a constant value of $N=2n+L$ and the radial-node number n of the molecular band depends on J as $n=(N-L)/2$. In addition, the deep double-folding potential gives rise to other molecular bands having different N values in each subchannel. The average energy interval between the molecular bands with different N values is about 10 MeV, which corresponds to the interval of $\Delta N=2$. In BCM, however, there is only one molecular band with $n=0$ in each subchannel because of the shallow depth of the nucleus-nucleus potential.

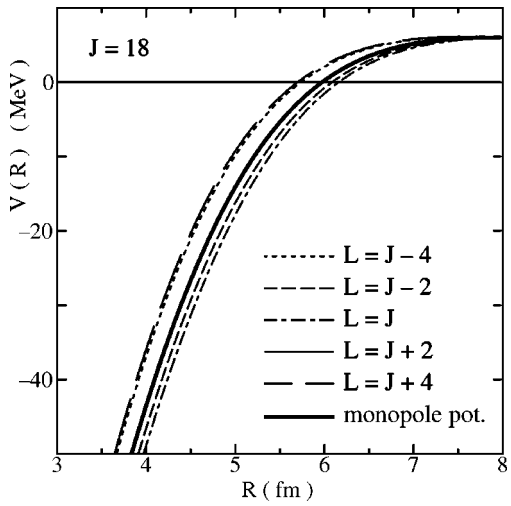

FIG. 6. The full potentials for the $[2_1^+\otimes 2_1^+]_{I=4,L}$ subchannel. The dotted, dashed, dotted-dashed, thin-solid, and long-dashed curves represent the full potentials for the $L=J-4$, $L=J-2$, $L=J$, $L=J+2$, and $L=J+4$ subchannels, respectively. The solid curve represents the monopole potential for the $2_1^+ + 2_1^+$ channel. The thin-solid curve cannot be distinguished from the solid one. The Coulomb potential is included in all the curves.

Next, we investigate the effect of the higher-multipole part of the folding potential originated from the nonspherical-density part, namely, the second term of the RHS in Eq. (14), on the molecular bands. Figure 6 shows the ''full potentials,'' which is the sum of the monopole and higher-multipole potentials, around the surface region for the five subchannels belonging to the $[2_1^+\otimes 2_1^+]_{I=4}$ channel. These potentials depend on J, as shown by Eq. (14), and we show the potential for $J=18$ in Fig. 6. The monopole potential for the channel is also shown by the solid curve in the same figure for comparison, which is independent of J. The addition of the higher-multipole potential to the monopole one gives rise to a visible change to the depth, depending on the subchannels. The difference between the monopole potential and the full one amounts to about 2–5 MeV around $R=4$ fm in all the subchannels except for the $L=J+2$ subchannel. The contribution of the higher-multipole potential depends on the subchannel and it is attractive in the $L=J$ and $L=J\pm 2$ subchannels, while it is repulsive in the $L=J\pm 4$ subchannels.

Figures 7(a) and 7(b) show the effective potentials composed of the nuclear, Coulomb, and centrifugal potentials for the $[2_1^+\otimes 2_1^+]_{I=4}$ channel. The nuclear and Coulomb part in (b) includes the contribution of the higher-multipole potential, while that in (a) does not include the contribution. The contribution from the higher-multipole part gives rise to about 5 MeV change of the pocket depth in $L\leqslant J$ the subchannels. In the $[2_1^+\otimes 2_1^+]_I$ channel with the channel spin $I=0$ and 2, the contribution of the higher-multipole part is similar to that of the $[2_1^+\otimes 2_1^+]_{I=4}$ channel, although it is not shown in the figures.

The molecular bands in Fig. 4(a) generated by the monopole potential are largely modified by the addition of the higher-multipole part. In Fig. 4(b), we show the $N=18$ mo-

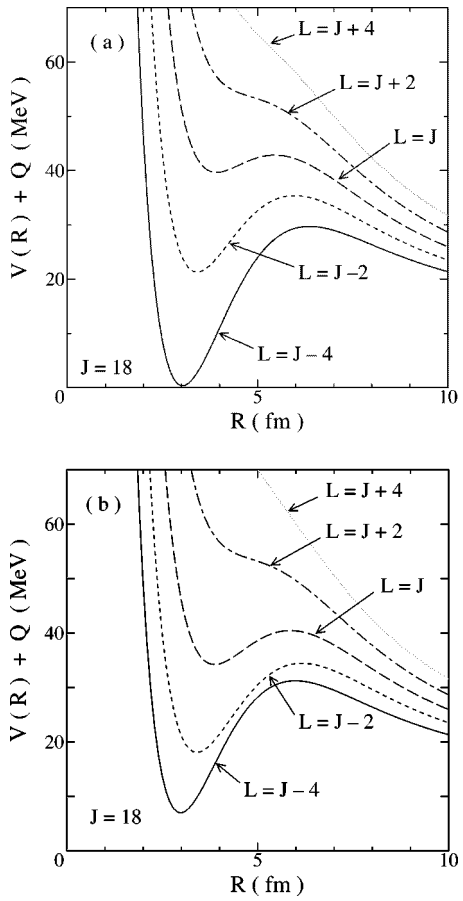

FIG. 7. The effective potentials, the sum of the nuclear Coulomb and centrifugal potentials (a) without and (b) with the nonspherical-density component of the nuclear potential, for $J=18$ in the $[2_1^+\otimes 2_1^+]_{I=4,L}$ subchannel. The solid, dotted, dashed-dotted-dashed, and thin-solid curves represent the effective potentials for the $L=J-4$, $L=J-2$, $L=J$, $L=J+2$, and $L=J+4$ subchannels, respectively.

lecular bands generated by the full potentials in the $[2_1^+\otimes 2_1^+]_{I=4}$ channels. The higher-multipole part contributes repulsively in the $L=J-4$, $L=J+2$, and $L=J+4$ subchannels, while it does so attractively in the $L=J-2$ and $L=J$ subchannels. Since the higher-multipole part depends on J [as seen in Eq. (14)], the energy shift of the molecular band due to the inclusion of the multipole part also depends on J. This change amounts to about 5 MeV, namely, the half of the energy interval between neighboring molecular bands with $\Delta N=2$. The large change of the energy position and slopes of the molecular bands in the $[2_1^+\otimes 2_1^+]_{I=4,L}$ subchannels results in a drastic change of the band-crossing diagram, as shown in Figs. 5(a) and 5(b). As seen in Fig. 5(a), only the most-aligned bands $[0_1^+\otimes 2_1^+]_{I=2,L=J-2}$ and $[2_1^+\otimes 2_1^+]_{I=4,L=J-4}$ cross with the elastic $(0_1^++0_1^+)$ band around $J=14$ and 16, respectively, in the case of monopole potential alone, while in the case with the higher-multipole part added the crossing region moves to $J=18$ as seen in Fig. 5(b), which is due to the repulsive effect of the higher-multipole part for the $L=J-I$ subchannels. In addition, the nonaligned bands such as $[0_1^+\otimes 2_1^+]_{I=2,L=J}$ and $[2_1^+\otimes 2_1^+]_{I=4,L=J-2}$ also cross with the elastic band at the same spin region. This is because the effect of the higher-multipole potential acts as an attractive effect to these subchannels.

These molecular bands modified by the higher-multipole part shown in Figs. 4(b) and 5(b) serve as the starting point of the subsequent coupled-channel calculations, in which the coupling among different channels are taken into account. It should be noted that the molecular bands generated by the monopole potential alone [shown in Figs. 4(a) and 5(a)] cannot be the starting point of the coupled-channel calculation.

It is worthwhile to discuss this point by comparing the present results with the previous BCM calculations [13–15] In the previous BCM calculation, the same kind of corrections corresponding to the higher-multipole part were also included in the potentials by the collective rotational model. However, the effect was small due to the use of a ''shallow optical potentials'' as the basic interactions. As a result, no difference was observed between the molecular bands generated by the monopole potential and that generated by the full potential as the starting point of their coupled-channel calculation. The main difference from the present paper, thus, exists in the interaction model adopted. Namely, in the present work, we adopt the double-folding-model interactions to construct the internucleus potentials and this interaction gives rise to a deep potential as well as a large component due to the higher-multipole part. Hence, in the present double-folding-model case, the starting point of the coupled-channel calculation is already very different from the band-crossing diagram based on the monopole potential shown in Fig. 5(a). In the next section, we perform the similar analyses for the cluster group (CG). In CG, the contribution from the higher-multipole part is very large and hence, the molecular bands generated by the monopole potentials are much more strongly modified by this part.

V. $3\alpha+3\alpha$ MOLECULAR BANDS

In this section, we discuss the folding potentials in the cluster group (CG) and discuss the behavior of the molecular bands generated by the potentials. In Fig. 8, we show the monopole potentials (nuclear+Coulomb) in the $0_2^++0_2^+$, $0_2^++2_2^+$, and $2_2^++2_2^+$ channels. From the comparison of Fig. 3 and Fig. 8, we can see that the interaction range of the potentials in all the CG channels is longer than that of the potentials in the SG channels. This is because the 0_2^+ and 2_2^+ states have a well-developed 3α cluster structure. In addition, one can see in Fig. 8 that there is a considerable difference in the interaction ranges among the above three channels. This is due to the fact that the density distribution of the 2_2^+ state has a longer range (i.e., the larger rms radius) than that of the 0_2^+ state, as we have already seen in Fig. 1.

Figure 9(a) shows the molecular bands in the $[2_2^+\otimes 2_2^+]_{I,L}$ subchannel with the channel spin $I=4$. All the molecular bands shown here are the members of the $N=20$ rotational band. The $0_2^++0_2^+$ molecular band is also shown in the same figure by open triangles with the dotted line. The moment of inertia of the $[2_2^+\otimes 2_2^+]_{I=4,L=J}$ molecular bands

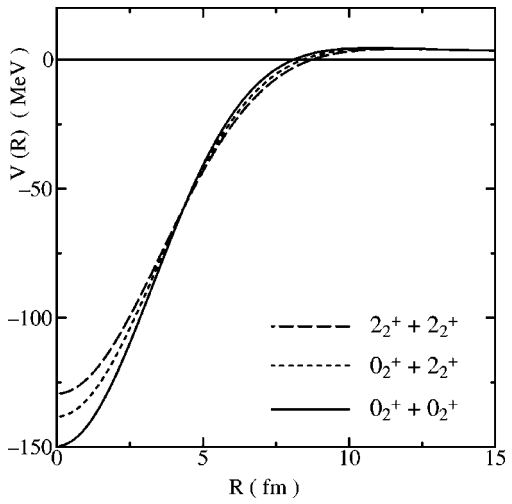

FIG. 8. The monopole part of the potentials in the $0_2^+ + 0_2^+$, $0_2^+ + 2_2^+$, and $2_2^+ + 2_2^+$ channels, which are shown by the solid, short-dashed, and long-dashed curves, respectively. The Coulomb part of the monopole potential is included in these potentials.

is much larger than that of the $[0_2^+ \otimes 0_2^+]$ ones, representing the fact that the interaction range of the $[2_2^+ \otimes 2_2^+]_{I=4}$ channel is much longer than that of the $[0_2^+ \otimes 0_2^+]$ channel. The energy positions of the $L \neq J$ bands are obtained by just shifting those of the $L=J$ band to the lower or higher J sides according to their L value, because the monopole nuclear+Coulomb interaction is common among the five subchannels.

The molecular bands with $L \leqslant J$ in the $[0_2^+ \otimes 2_2^+]_{I=2,L}$ and $[2_2^+ \otimes 2_2^+]_{I=4,L}$ subchannels are plotted together in Fig. 10(a). The $0_2^+ + 0_2^+$ molecular band is also plotted by the double circles for comparison. It is seen that the ''band crossing'' between the aligned molecular bands and the $0_2^+ + 0_2^+$ one occurs around $J=14$ and 18.

Next, we investigate the effect of inclusion of the higher-multipole part on the molecular bands. The change of the potential due to the higher-multipole part is more prominent in the $[2_2^+ \otimes 2_2^+]_{I=4}$ channel because of the large deformation of ^{12}C in the 2_2^+ state. Figure 11 shows the full potentials for $J=18$ in the $[2_2^+ \otimes 2_2^+]_{I=4}$ subchannel around the surface region. The contribution of the higher-multipole part depends on the subchannel and it is attractive in the $L=J \pm 4$ subchannels, while it is repulsive in other subchannels. The higher-multipole part has opposite sign from that in the $[2_1^+ \otimes 2_1^+]_{I=4}$ channel. This is because the sign of the quadrupole component of the 2_2^+ density is opposite from that of the 2_1^+ density, which may reflect the difference of deformation type, namely, an oblate shape in the 2_1^+ state and a prolatelike shape in the 2_2^+ one [28–31]. The deviation of the full potential from the monopole one is particularly large in the $L=J \pm 4$ subchannels, which amounts to about 10 MeV around $R=7$ fm, which is much larger than the corresponding correction in the $[2_1^+ \otimes 2_1^+]_{I=4}$ channels.

In Figs. 12(a) and 12(b), we compare the effective potentials with and without the higher-multipole part, respectively, in the $[2_2^+ \otimes 2_2^+]_{I=4,L}$ subchannel. The contribution from the

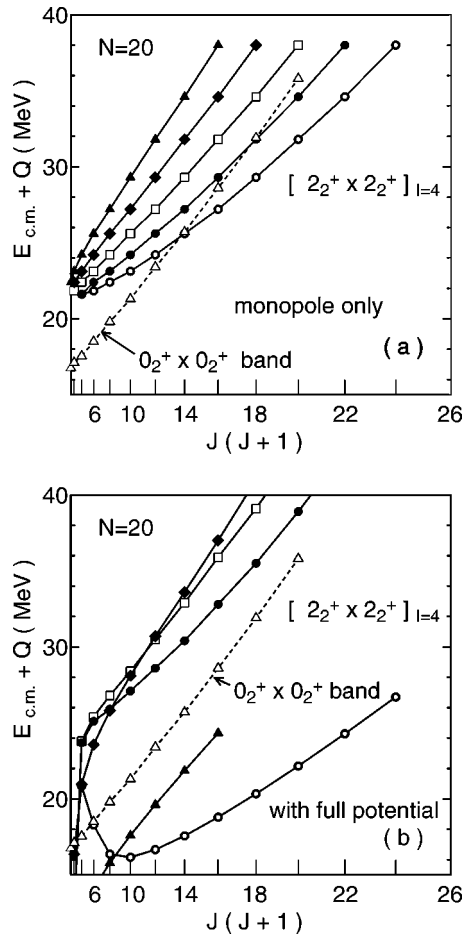

FIG. 9. (a) The molecular bands of the $[2_2^+ \otimes 2_2^+]_{I=4,L}$ subchannel generated monopole potentials. The double circles, solid circles, open squares, solid diamonds, and solid triangles represent the band in the $L=J-4$, $L=J-2$, $L=J$ and $L=J+2$, $L=J+4$ subchannels, respectively. (b) The same as (a) but for the molecular bands calculated from the full potentials. In both figures, the $[0_2^+ \otimes 0_2^+]$ molecular band is also shown by the short-dashed line marked by the open triangles.

higher-multipole part gives rise to a large change to the pocket depth and the barrier height in all the subchannels. In particular, the barrier height and the pocket depth are drastically changed in the $L=J \pm 4$ subchannels. It is interesting that the pocket depth of the $L=J+4$ subchannel becomes deeper than that of the $L=J$ and $L=J+2$ subchannels.

As we have confirmed, the correction due to the higher-multipole potential is very large and, hence, the molecular bands generated by the monopole potential must be also strongly modified. The $[2_2^+ \otimes 2_2^+]_{I=4}$ molecular bands calculated by the full potentials are shown in Fig. 9(b). All the molecular bands are members of the $N=20$ band. The location of the molecular bands calculated with the full potentials drastically changes from that calculated with the monopole potentials.

From the comparison of Figs. 4(b) and 9(b), the correction due to the higher-multipole part is much larger for the $[2_2^+ \otimes 2_2^+]_{I=4}$ channels than the $[2_1^+ \otimes 2_1^+]_{I=4}$ ones. The effect contributes attractively to the $L=J \pm 4$ subchannels,

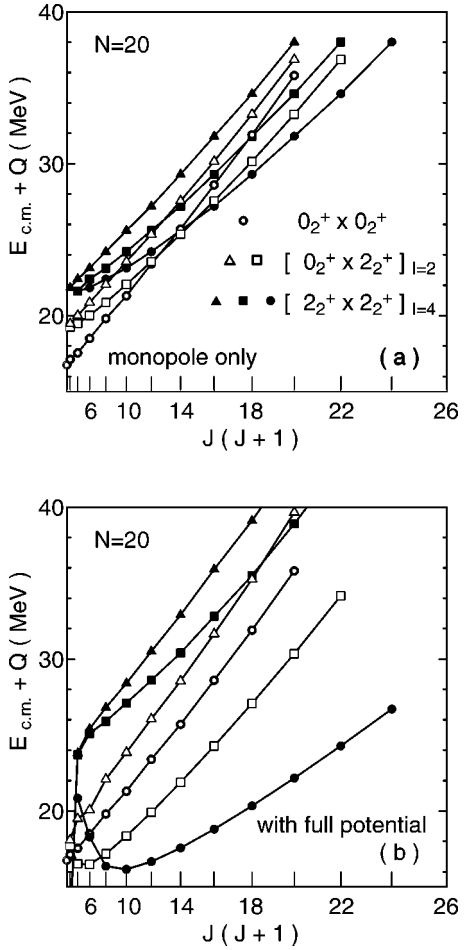

FIG. 10. (a) The molecular bands in the $[0_2^+ \otimes 0_2^+]$ (double circles), $[0_2^+ \otimes 2_2^+]_{I=2,L=J-2,J}$ (open squares, open triangles), and $[2_2^+ \otimes 2_2^+]_{I=4,L=J-4,J-2,J}$ (solid circles, solid squares, solid triangles) subchannels. All the molecular bands are calculated from the monopole potentials. (b) The same as (a) but for the molecular bands calculated from the full potentials.

while repulsively to other subchannels. In particular, the effect is the largest in the $L=J\pm 4$ subchannels, which induces about 10 MeV energy gain. It also reaches about 5 MeV for other subchannels except for the low spins ($J\leqslant 6$). Since the higher-multipole part depends on J, the energy shift of the molecular band also depends on J. In the low-spin ($J\leqslant 4$) region, the individual bands have a strange behavior.

As shown in the above figure, the contribution from the higher-multipole part gives rise to a large energy shift in the $[2_2^+ \otimes 2_2^+]_{I=4}$ channels. Therefore, the band-crossing diagram between the $0_2^+ + 0_2^+$ molecular band and the aligned bands in the $[0_2^+ \otimes 2_2^+]_{I=2}$ and $[2_2^+ \otimes 2_2^+]_{I=4}$ channels generated by the monopole potentials, shown in Fig. 10(a), is largely modified by the contribution of the higher-multipole part. In Fig. 10(b), the $L\leqslant J$ molecular bands in the $[0_2^+ \otimes 2_2^+]_{I=2,L}$ and $[2_2^+ \otimes 2_2^+]_{I=4,L}$ subchannels are plotted. The $0_2^+ + 0_2^+$ molecular band is also plotted in the same figure by the double circles which are connected by the dashed line.

In the calculation with the monopole potentials alone shown in Fig. 10(a), we see that only the three aligned bands

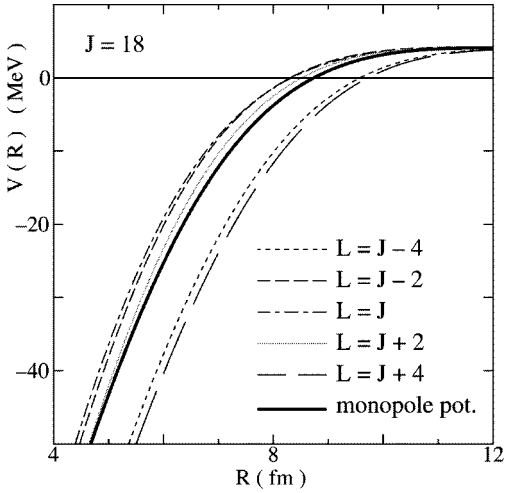

FIG. 11. The full potentials for the $[2_2^+ \otimes 2_2^+]_{I=4,L}$ subchannel. The dotted, dashed, dotted-dashed, thin-solid, and long-dashed curves represent the full potentials for the $L=J-4$, $L=J-2$, $L=J$, $L=J+2$, and $L=J+4$ subchannels, respectively. The solid curve represents the monopole potential for the $2_2^+ + 2_2^+$ channel. The thin line cannot be distinguished from the solid one. The Coulomb part is also included in all the potentials.

$[0_2^+ \otimes 2_2^+]_{I=2,L=J-2}$ and $[2_2^+ \otimes 2_2^+]_{I=4,L}$ (with $L=J-4$ and $L=J-2$), cross with the $0_2^+ + 0_2^+$. In the case with the higher-multipole contribution shown in Fig. 10(b), the band-crossing diagram of Fig. 10(a) is completely distorted by the large correction of the higher-multipole part. This implies that the starting point of the coupled-channel calculation is the diagram of Fig. 10(b), which is completely different from the band-crossing diagram of Fig. 10(a).

VI. CHANNEL COUPLING EFFECT ON THE $^{12}C+^{12}C$ MOLECULAR BANDS

In this section, we discuss the coupled-channel effects on the molecular bands of shell group shown in the preceding section. In order to see the nuclear structure of the resonance states more clearly, we do not include the imaginary potentials also in the CC calculation. The coupling potentials between different subchannels $\alpha L \neq \beta L'$ are calculated from the nondiagonal transition densities. Both the strength of the higher-multipole part and that of the nondiagonal transition densities depends on the deformation of the ^{12}C nucleus.

Figure 13 shows the energy dependence of the partial-wave components of the total cross section divided by $\pi k^{-2}(2J+1)$, namely, $k^2\pi^{-1}(2J+1)^{-1}\sigma_{\rm tot}^{(J)}=2(1-{\rm Re}\,S_{\rm el}^{(J)})$. The solid curves are the results of the CC calculation. The results of the single-channel calculation with all the coupling to the ^{12}C excitation switched off are also shown by the dotted curves for comparison. In the single-channel calculation, a potential resonance is generated around the barrier-top energy of each partial wave. The sequence of the potential resonances forms a molecular band with $N=2n+L=18$ and, hence, the band terminates at $J=18$. A sign of the appearance of $N=20$ band is also seen at several MeV above the $N=18$ band but it is unclear, because

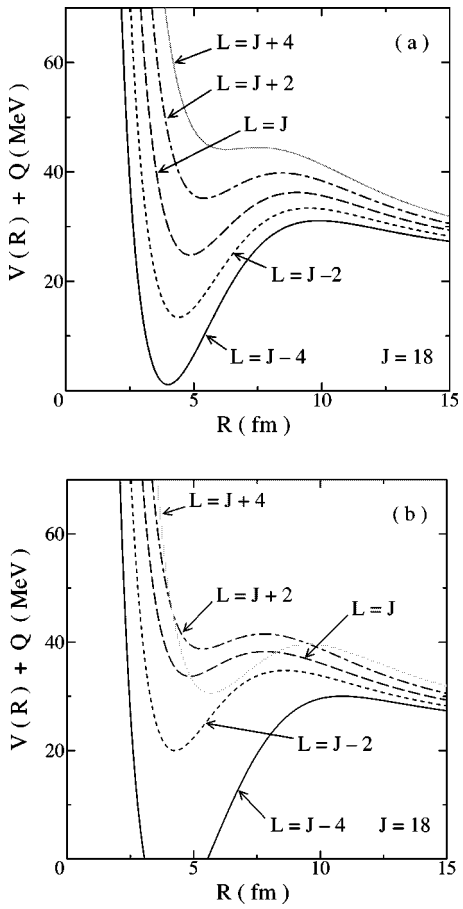

FIG. 12. The effective potentials composed of the nuclear Coulomb and centrifugal potentials (a) without and (b) with the nonspherical-density component of the nuclear potential, for $J=18$ in the $[2_2^+ \otimes 2_2^+]_{I=4,L}$ subchannel. The solid, dotted, dashed-dotted-dashed, and thin-solid curves represent the effective potentials for the $L=J-4$, $L=J-2$, $L=J$, $L=J+2$, and $L=J+4$ subchannels, respectively.

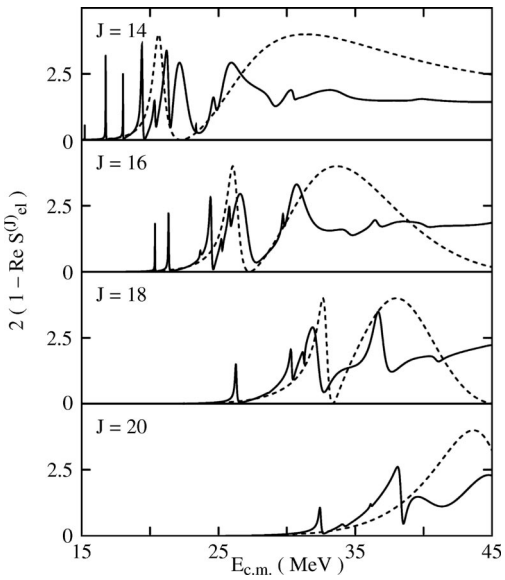

FIG. 13. Partial-wave components of the total cross section divided by $\pi k^{-2}(2J+1)$ for $J=14$ to 20 obtained within the model space consisting of the shell-group channels. The dotted curves are the results of the single channel calculation with no channel coupling, while the solid ones are the results of the coupled-channel calculation.

it lies well above the barrier-top energies and the resonance states have large widths. The channel coupling to the 2_1^+ state of ^{12}C gives rise to a number of sharp resonances in all the partial waves investigated. In particular, the structure becomes more complicated in the lower partial wave than in the higher partial wave, because the entrance wave can enter into well inside the barrier-top region, where the coupling potentials are very strong.

In order to understand the detailed properties of the resonance wave functions, we calculate the following two kinds of quantities: first, the probability of finding the system in subchannel component, which is represented by the squared modulus of the subchannel wave functions integrated over the whole radial range, and, second, the number of the radial nodes n or the total oscillator-quantum number $N=2n+L$, of the radial wave function in each subchannel component. However, since the resonance state is a scattering state, its wave function cannot be normalized to unity and, hence, the absolute probability and the number of radial nodes cannot be defined for the scattering-state wave functions. Therefore, we employ a ''bound-state-like approximation'' for solving the coupled-channel equations. In this approximation, the coupled-channel equations are solved by the variational method in the ''bound-state-like'' boundary condition using the L^2-integrable basis functions. Namely, the radial wave functions in the individual subchannels $\chi^{(J)}_{\beta L'}$ are expanded in terms of L^2-integrable basis functions and the expansion coefficients are obtained by solving the eigenvalue equations. Using the approximated wave functions, we can evaluate the probability and the number of the radial nodes.

Figure 14 shows the probability of finding the system in various subchannels obtained by the bound-state approximation, which is normalized to unity in each eigenstate. In the figure, we show the probability for some important subchannels of a spin-orbit aligned configuration in the case of $J=16$. The solid circles in the lowest column are the energy eigenvalues (energy spectra) obtained by the bound-state approximation. The partial cross section for $J=16$ obtained by the corresponding calculation in the scattering-state boundary condition is also shown in the lowest column in Fig. 14. As shown by the arrows, all the energy positions calculated by the bound-state approximation appear at high-energy side by about 1 MeV compared with those of the resonance states obtained by the exact scattering-states calculation. This is because the system is confined in a finite region in the bound-state approximation.

It is clearly seen that each eigenstate (or corresponding resonance state) has its own characteristic channel structure, namely, the probability distribution among the subchannels. For example, the sharp resonance at $E_{\mathrm{c.m.}}=21.36$ MeV, whose corresponding bound state exists at $E_{\mathrm{c.m.}}=22.2$ MeV, has two dominant components, the elastic-channel component and the $L=J-2$ component of the $[0_1^+ \otimes 2_1^+]_{I=2}$ single-excitation channel, while a broad resonance

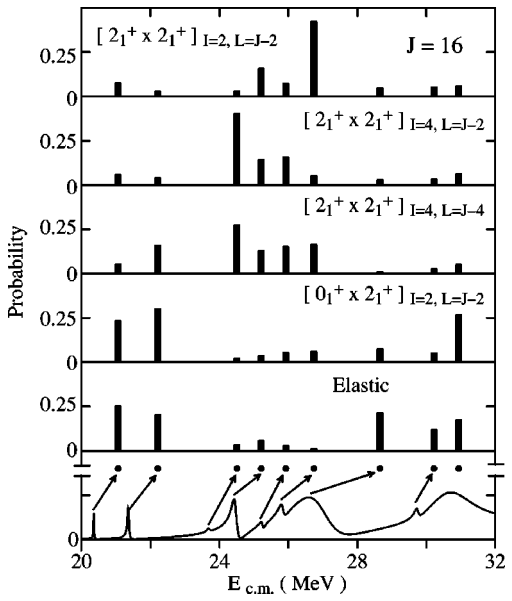

FIG. 14. Channel component of wave functions for each resonance in $J=16$. The solid circles show the energy value of the eigenstates obtained by the bound-state approximation. The individual ordinate represents the probability of each subchannel component. The partial cross section for $J=16$ is also in the lowest panel. See text for details.

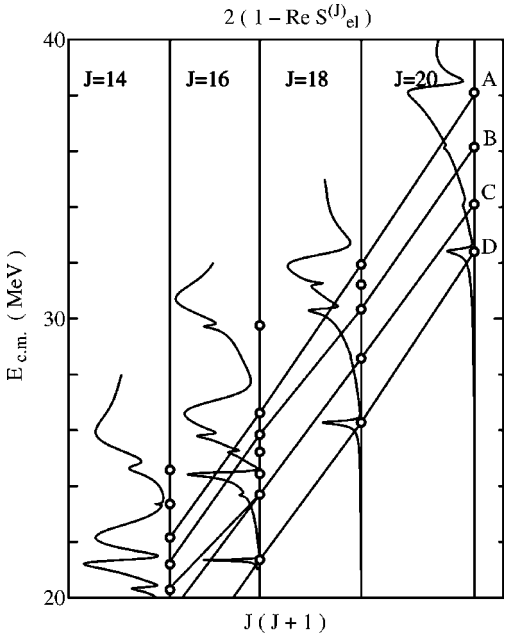

FIG. 15. The diagram of the rotational spectra, called ''eigenbands,'' in SG drawn in $E-J$ plane. The ordinate and the abscissa represent the total energy of the $^{12}C+^{12}C$ system and the $J(J+1)$ values. The double circles show the resonance-energy positions. The resonance states connected by a solid line, corresponding to the eigenbands, have a common subchannel structure, i.e., a dominant component. The four eigenbands are identified, which are labeled by $A\sim D$. The energy dependence of the total cross sections, $2(1-\mathrm{Re}\,S_{el}^{(J)})$, are also drawn to show the peak energy and the width of the individual resonances. See text for details.

at $E_{\mathrm{c.m.}}=26.58$ MeV has the large elastic-channel component, etc. The radial node number n of the dominant subchannels in the individual resonance states can be evaluated by taking the overlap between the wave function in the CC calculation and that in the single-channel calculation without the channel coupling.

We have performed the same kind of analysis of the resonance wave functions for other partial waves and classified the resonance states according to the subchannel structure and the radial node of the dominant subchannel components. As a result, we have identified several rotational bands. Figure 15 shows the rotational bands thus obtained for grazing partial waves ($J=14-20$). The resonance states connected by the solid line have a common subchannel structure, namely, the dominant subchannel components are common to all the states belonging to the same band. The total oscillator-quantum number $N=2n+L$ is also common to all the states in a band. The four rotational bands are identified, which are labeled by A–D. The energy dependence of the total cross sections $2(1-\mathrm{Re}\,S_{el}^{(J)})$, are also drawn to show the peak energy and the width of the individual resonances.

We call the rotational bands consisting of the eigenstates (the solutions of the CC equations) the ''eigenbands.'' In Table I, we show the dominant subchannel components and N values for each eigenband of Fig. 15. The average population of the dominant subchannel component in each eigenband is also listed in the right-most column of the same table. The population of the dominant components are less than 50%, which also suggests a rather strong channel coupling among SG.

These eigenbands are plotted again in Fig. 16(a) together with the dominant subchannels, which are labeled by symbols indicated, and their N values. The single-channel bands with $N=16-20$ are also plotted in Fig. 16(b) for comparison. It is seen that the energy positions of the eigenbands with $N=18$ (bands B, C, D) are close to those of the single-channel bands with $N=16$, while the energy positions of the eigenbands with $N=20$ (band A) are close to those of the single-channel bands with $N=18$. This implies that, due to the channel coupling effect, the original single-channel bands are pulled down by about 6–10 MeV, which corre-

TABLE I. Dominant subchannels in the individual eigenbands for SG.

Band	Subchannel	N	%
A	$[0_1^+\otimes 2_1^+]_{I=2,L=J}$	20	35.6
	elastic	20	19.5
B	$[2_1^+\otimes 2_1^+]_{I=2,L=J-2}$	18	47.1
C	$[2_1^+\otimes 2_1^+]_{I=4,L=J-4}$	18	28.4
	$[2_1^+\otimes 2_1^+]_{I=4,L=J-2}$	18	36.3
D	$[0_1^+\otimes 2_1^+]_{I=2,L=J-2}$	18	30.5
	elastic	20	20.2

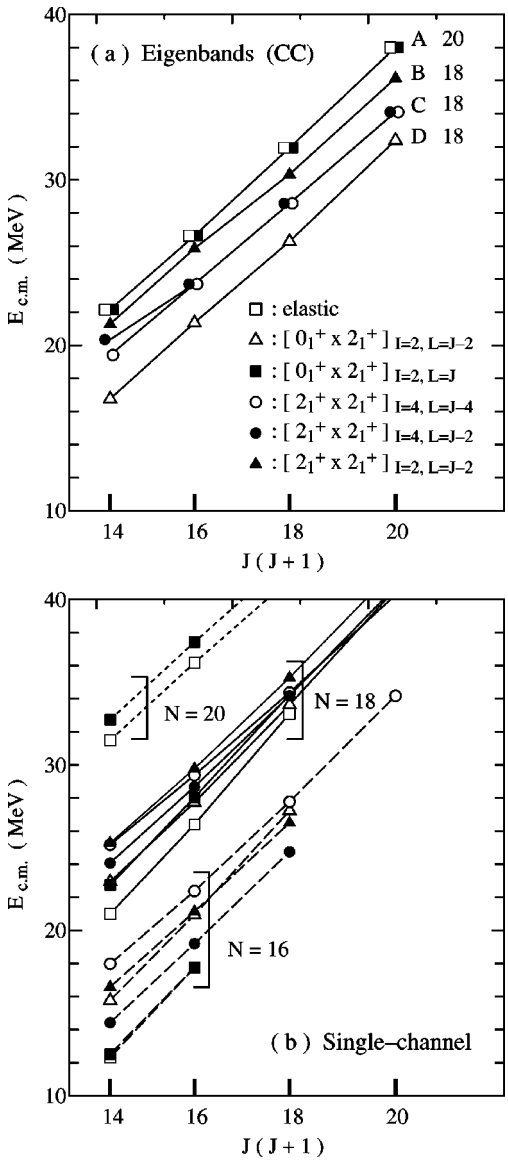

FIG. 16. Comparison of energy position of the single-channel bands with that of eigenbands obtained by the CC calculation. (a) The energy positions of the eigenbands A–D. In (a), N values of the dominant subchannels are also shown. (b) The energy positions of the molecular bands with $N=16$ to 20, which are obtained by the single-channel calculation with the full potential in the bound-state approximation. In both figures, the open squares, open triangles, and solid squares represent the elastic, $[0_1^+\otimes 2_1^+]_{I=2,L=J-2}$, and $[0_1^+\otimes 2_1^+]_{I=2,L=J}$ subchannels, respectively, while the open and solid circles represent the $[2_1^+\otimes 2_1^+]_{I=4,L=J-4}$ and $[2_1^+\otimes 2_1^+]_{I=4,L=J-2}$ subchannels, respectively. The solid triangles show the $[2_1^+\otimes 2_1^+]_{I=2,L=J-2}$ subchannels.

spond to the energy interval between the molecular bands with $\Delta N=2$.

In this way, the channel-coupling effects among the shell group are not very weak but rather strong. This result is very different from the channel coupling scheme in the weak coupling model such as BCM [13–15]. Since the channel coupling studied in BCM was very weak, the mixing of the different channels is very small except for the band crossing region and, hence, the overall energy gain by the channel coupling is almost negligible in the whole energy-spin region. In the present CC calculation based on the double folding interaction, however, the strong channel mixing occurs in all the grazing partial waves and the energy shift induced by the channel coupling is also large, even at non-band-crossing region.

As seen in Table I, the probabilities of the dominant components somewhat depend on the subchannels. For instance, it is relatively large for subchannels with an aligned L value such as the $[2_1^+\otimes 2_1^+]_{I=4,L=J-4}$ one, while it is small for subchannels such as the elastic and $[0_1^+\otimes 2_1^+]_{I=2,L=J}$ ones with a nonaligned L value. Moreover, there is no dominant subchannel with $L>J$, i.e., the antialigned L. These results suggest that the channel coupling effect is relatively weak for subchannels with aligned L than for subchannels with nonaligned L. The stability of the subchannel with aligned L against the channel coupling is due to the weakness of the centrifugal potential. In the aligned subchannel, the pocket depth of the effective potential becomes deep and the unperturbed wave function obtained by the single channel calculation becomes a higher nodal state. The higher-nodal nature of the wave function leads to a reduction of overlap integral of the coupling potentials and the wave function, which results in a weakening of the channel-coupling effect.

One may also notice that the probability of the elastic channel is the smallest of all the dominant subchannels, of which average value is less than about 20%, while all the other subchannel components have the probability of more than about 30%. The reason is that the elastic channel strongly reduced by the channel coupling can also be interpreted by the intrinsic structure of the ^{12}C nucleus. The channel coupling can be related with the deformation of the two colliding nuclei in their body-fixed frames. The intrinsic shape of ^{12}C is strongly deformed in an oblate shape [28,29]. The 0_1^+ ground state of ^{12}C corresponds to a rotational state in which the intrinsically deformed nucleus rotates spherically. When such deformed nuclei get closer, the location of the local minimum in the adiabatic potential-energy surface strongly depends on the relative distance and the orientation of the colliding nuclei [46,47]. For example, the equator-equator configuration becomes stable at relatively long distance, while the pole-pole configuration becomes stable at a shorter distance. In such a situation, it may not be plausible to expect that both of the interacting two ^{12}C nuclei rotate spherically in a very deformed adiabatic-potential surface. Therefore, the elastic $[0_1^+\otimes 0_1^+]$ component will be strongly suppressed.

VII. SUMMARY AND DISCUSSION

In this paper, we showed the expression of the microscopic DF potential and discussed its properties based on the multipole expansion of the nucleon densities. According to the multipole expansion, the nucleon density of a state with a nonzero spin can be divided into the monopole part and the multipole one. The former and latter parts correspond to spherical and nonspherical component of the density, respec-

tively. The density of a spinless state has only the monopole component.

The DF potentials, namely the diagonal potentials, can also be divided into two parts according to the multipolarity of the density. The one part is calculated by folding the monopole densities, while the other part is given by folding the nonzero multipole components. The latter part of the potential exists in the channels with a nonzero intrinsic spin. We referred to the former and latter parts of the potentials as ''monopole potential'' and ''higher-multipole potential,'' respectively. The former potential does not depend on the channel spin *I*, the relative angular momentum *L*, or the total one *J*, while the latter potential depends on *I*, *L*, and *J*. Therefore, the nucleus-nucleus interactions of the different subchannels are different from each other even though they consist of a common intrinsic-state channel for given *J*. It should be noticed that the properties of the DF potentials shown in this paper are quite general, because they are determined by the multipolarity of densities. In the present framework, the monopole and higher-multipole potentials are completely determined once we have a set of nucleon densities.

We applied the above discussion to the $^{12}C+^{12}C$ system. It was found that the higher-multipole potentials are especially large for the channels in which both ^{12}C nuclei are excited to the 3α states. The $3\alpha+3\alpha$ molecular bands generated by the monopole potentials are largely modified due to the large contribution of the higher-multipole ones. The sequence of the barrier-top resonances generated by the monopole potentials forms the band crossing between the molecular band of the $[0_2^+\otimes 0_2^+]$ channel and those of the aligned $[0_2^+\otimes 2_2^+]_{I,L}$ and $[2_2^+\otimes 2_2^+]_{I,L}$ subchannels. However, the contribution from the higher-multipole potentials drastically changes the location of the individual molecular bands calculated by the monopole potentials and, hence, the characteristics of the band crossing is largely modified as shown in Fig. 10. The large correction due to the multipole densities originates from the fact that the 3α states in ^{12}C have a large prolatelike deformation. (The average quadrupole-deformation parameter for the 3α states is known to be about $\beta_2\simeq+1.6$ [31].)

In the $^{12}C+^{12}C$ channels, the effect of the higher-multipole potentials is a little moderate compared with that in the $3\alpha+3\alpha$ channels. The effect induces a non-negligible modification about 2–5 MeV energy gain of the molecular bands in the excited 2_1^+ channels generated by the monopole potential alone, as shown in Figs. 4 and 5. It should be noticed that these properties about the potentials and the molecular bands are very different from those discussed in the BCM studies [13–15]. In the present DF potential, the starting point of the coupled-channel calculation is not the molecular bands calculated by the monopole potentials but the modified bands with the effect of the higher-multipole potentials included. In the previous BCM calculations, the same kind of corrections corresponding to the higher-multipole potentials are included by the use of the collective rotational model, but their effect was negligible due to the use of the ''shallow optical potentials'' as basic nucleus-nucleus interactions. As the result, the starting diagram for the coupled-channel calculations was almost identical to the band-crossing diagram generated by the monopole potentials.

Moreover, the effect of channel-coupling among the different channels is also important and it gives rise to an additional energy gain of about 6–10 MeV. Due to this energy shift, the resonance wave functions have an additional radial node compared with those of the original single-channel resonances existing in the same energy region as shown in Fig. 16. We called the new bands generated by the channel coupling the ''eigenbands.'' There is observed a considerable mixing among the subchannels and the population of the dominant subchannel component in the eigenbands is about 20–50 %. Since the channel coupling is rather strong, the reaction mechanism leading to the resonance formation is very different from the ''weak-coupling picture'' suggested by BCM [13–15]. The possibility of the strong-coupling states in the $^{12}C+^{12}C$ molecular resonances was also suggested by the ''strong coupling model'' based on the modified-perturbed-stationary state approximation [48,49].

In order to examine the reliability of the strong channel-coupling effect due to DF potential more clearly, we should calculate the spin alignment of the $^{12}C+^{12}C$ inelastic scattering [50,51]. The BCM has not succeeded in reproducing the spin alignment in the $^{12}C+^{12}C$ inelastic scattering [52]. Therefore, it is very interesting to discuss the spin alignment using the coupled-channel calculation based on the present DF-model potential. The analysis of the spin alignment is now in progress. The channel coupling effects on the $3\alpha+3\alpha$ and $^{12}C+3\alpha$ bands are expected to be much stronger than those we saw in the $^{12}C+^{12}C$ channels because of the strong deformation of the 3α states of ^{12}C. The channel-coupling effect and the reaction mechanism for the formation of the resonances in the $^{12}C+3\alpha$ and $3\alpha+3\alpha$ channels will be discussed in a forthcoming paper.

ACKNOWLEDGMENTS

The authors would like to thank Y. Abe and K. Katō for valuable discussions and critical comments. The authors also would like to thank M. Kamimura for providing us with the transition densities of the ^{12}C nucleus including the unpublished ones.

[1] E. Almqvist, D. A. Bromley, and J. A. Kuehner, Phys. Rev. Lett. **4**, 515 (1960).

[2] See, for example, K. A. Erb and D. A. Bromley, *Treatise of Heavy-Ion Science 3* (Plenum, New York, 1985), p. 201.

[3] T. M. Cormier *et al.*, Phys. Rev. Lett. **38**, 940 (1977).

[4] T. M. Cormier *et al.*, Phys. Rev. Lett. **40**, 924 (1977).

[5] B. R. Fulton, T. M. Cormier, and B. J. Herman, Phys. Rev. Lett. **38**, 940 (1977).

[6] A. Morsad, F. Haas, C. Beck, and R. M. Freeman, Z. Phys. A **353**, 43 (1995).

[7] S. Szilner, Z. Basrak, R. M. Freeman, F. Haas, A. Morsad, and C. Beck, Phys. Rev. C **55**, 1312 (1997).
[8] S. Szilner, Z. Basrak, R. M. Freeman, F. Haas, A. Morsad, M. P. Nicoli, and C. Beck, J. Phys. G **25**, 1 (1999).
[9] L. R. Greenwood *et al.*, Phys. Rev. C **12**, 156 (1975).
[10] N. R. Fletcher *et al.*, Phys. Rev. C **13**, 1173 (1976).
[11] H. T. Fortune, S. C. Headley, and L. R. Medsker, Phys. Rev. C **14**, 1271 (1976).
[12] D. R. James and N. R. Fletcher, Phys. Rev. C **17**, 2248 (1978).
[13] Y. Abe, *Nuclear Molecular Phenomena*, edited by N. Cindro (North Holland, Amsterdam, 1978).
[14] Y. Kondō, Y. Abe, and T. Matsuse, Phys. Rev. C **19**, 1356 (1979).
[15] Y. Abe, Y. Kondō, and T. Matsuse, Suppl. Prog. Theor. Phys. **68**, 303 (1980).
[16] T. Matsuse, Y. Abe, and Y. Kondō, Prog. Theor. Phys. **59**, 1904 (1978).
[17] T. Tazawa, J. Y. Park, and Y. Abe, Phys. Lett. **125B**, 30 (1983).
[18] Y. Kondō, D. A. Bromley, and Y. Abe, Phys. Rev. C **22**, 1068 (1980).
[19] H. J. Fink, W. Scheid, and W. Greiner, Nucl. Phys. **A188**, 259 (1972).
[20] J. Park, W. Greiner, and W. Scheid, Phys. Rev. C **16**, 2276 (1977).
[21] O. Tanimura and T. Tazawa, Phys. Lett. **105B**, 334 (1981).
[22] L. E. Cannell, R. W. Zurmuhle, and D. P. Balamuth, Phys. Rev. Lett. **43**, 837 (1979).
[23] T. Wada and H. Horiuchi, Prog. Theor. Phys. **80**, 488 (1988).
[24] T. Wada and H. Horiuchi, Prog. Theor. Phys. **80**, 562 (1988).
[25] Y. Kondō, B. A. Robson, and R. Smith, Phys. Lett. B **227**, 310 (1989); Y. Kondō, F. Michel, and G. Reidemeister, *ibid.* **242**, 340 (1990); M. E. Brandan and G. R. Satchler, Phys. Rep. **285**, 143 (1997), and reference therein.
[26] A. H. Wuosmaa, R. R. Betts, B. B. Back, M. Freer, B. G. Glagola, Th. Happ, D. J. Henderson, P. Wilt, and I. G. Bearden, Phys. Rev. Lett. **68**, 1295 (1992).
[27] A. H. Wuosmaa, M. Freer, B. B. Back, R. R. Betts, J. C. Gehring, B. G. Glagola, Th. Happ, D. J. Henderson, P. Wilt, and I. G. Bearden, Phys. Rev. C **50**, 2909 (1994).
[28] E. Uegaki, S. Okabe, Y. Abe, and M. Tanaka, Prog. Theor. Phys. **57**, 1262 (1977).
[29] E. Uegaki, S. Okabe, Y. Abe, and M. Tanaka, Prog. Theor. Phys. **62**, 1621 (1979).
[30] Y. Fukushima and M. Kamimura, *Proceedings of the International Conference Nuclear Structure* [J. Phys. Soc. Jpn. **44**, 225 (1977)].
[31] M. Kamimura, Nucl. Phys. **A351**, 456 (1981).
[32] S. P. G. Chappell, D. L. Watson, S. P. Fox, C. D. Jones, W. D. M. Rae, P. M. Simmons, M. Freer, B. R. Fulton, N. M. Clarke, N. Curtis, M. J. Leddy, J. S. Pople, S. J. Hall, R. P. Ward, G. Tungate, W. N. Catfold, G. J. Gyapong, S. M. Singer, and P. H. Regan, Phys. Rev. C **51**, 695 (1995).
[33] R. A. Le Marechal, N. M. Clarke, M. Freer, B. R. Fulton, S. J. Hall, S. J. Hoath, G. R. Kelly, R. P. Ward, C. D. Jones, P. Lee, and D. L. Watson, Phys. Rev. C **55**, 1881 (1997).
[34] B. R. Fulton, T. M. Cormier, and B. J. Herman, Phys. Rev. C **21**, 198 (1980).
[35] S. F. Pate, R. W. Zurmühle, P. H. Kutt, and A. H. Wuosmaa, Phys. Rev. C **37**, 1953 (1988).
[36] Y. Hirabayashi, Y. Sakuragi, and Y. Abe, Phys. Rev. Lett. **74**, 4141 (1995).
[37] Y. Sakuragi, M. Ito, M. Katsuma, M. Takashina, Y. Kudo, Y. Hirabayashi, S. Okabe, and Y. Abe, in *Proceedings of the 7th International Conference on Clustering Aspects of Nuclear Structure and Dynamics*, edited by M. Korolija, Z. Basrak, and R. Caplar (World Scientific, Singapore, 2000), p. 138.
[38] M. Ito, Y. Sakuragi and Y. Hirabayashi, Few-Body Syst., Suppl. **12**, 137 (2000).
[39] G. R. Satchler and W. G. Love, Phys. Rep. **55**, 183 (1979).
[40] A. M. Kobos, B. A. Brown, R. Lindsay, and G. R. Satchler, Nucl. Phys. **A384**, 65 (1982); A. M. Kobos, B. A. Brown, P. E. Hodgson, G. R. Satchler, and A. Budzanowski, *ibid.* **A425**, 205 (1984); M. E. Brandan and G. R. Satchler, *ibid.* **A487**, 477 (1988).
[41] M. El-Azab Farid and G. R. Satchler, Nucl. Phys. **A438**, 525 (1985).
[42] G. Bertsch, J. Borysowicz, H. McManus, and W. G. Love, Nucl. Phys. **A284**, 395 (1977).
[43] J. P. Jeukenne, A. Lejeune, and C. Mahaux, Phys. Rev. C **16**, 80 (1977).
[44] G. R. Satchler, *Direct Nuclear Reactions* (Clarendon, Oxford 1983).
[45] M. Ito, Y. Sakuragi, and Y. Hirabayashi, Eur. Phys. J. A **5**, 373 (1999).
[46] E. Uegaki and Y. Abe, Phys. Lett. B **231**, 28 (1989).
[47] E. Uegaki and Y. Abe, Prog. Theor. Phys. **90**, 615 (1993).
[48] O. Tanimura and T. Tazawa, Phys. Rep. **61**, 253 (1980).
[49] M. Nogami, in Proceedings of the INS-IPCR Symposium on Cluster Structure of Nuclei and Transfer Reactions Induced by Heavy Ion, Tokyo, 1975, p. 401.
[50] S. J. Willet *et al.*, Phys. Rev. C **28**, 1986 (1983).
[51] W. Trombik *et al.*, Phys. Lett. **135B**, 271 (1984); Comments Nucl. Part. Phys. **13**, 266 (1984); Z. Phys. A **296**, 187 (1980).
[52] O. Tanimura and U. Mosel, Phys. Lett. **114B**, 7 (1982).